Solar Energy 279 (2024) 112777

Contents lists available at ScienceDirect

Solar Energy

journal homepage: www.elsevier.com/locate/solener

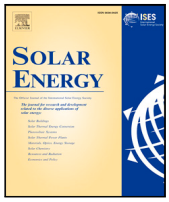

Design and analysis of an efficient crystalline silicon-based thin-film solar cell inspired by *Chlamydomonas reinhardtii*

Abdul Ahad Mamun, Jawadul Karim, Muhammad Anisuzzaman Talukder *

Department of Electrical and Electronic Engineering, Bangladesh University of Engineering and Technology, Dhaka 1205, Bangladesh

ARTICLE INFO

Keywords:
Photovoltaics
Bio-inspired solar cells
Nanophotonics
Thin-film solar cell
Crystalline silicon

ABSTRACT

In photovoltaic (PV) solar cells, the photo-absorbing structure should absorb solar energy optimally to convert it into electrical power efficiently. The major criteria for sustainable PV technology are using low-cost photo-absorbing material and thin-film structures with efficient optical and electrical performances. We propose a monomer and trimer array-based heterogeneous nanopillar (MTHN) structure for efficient light absorption inspired by *Chlamydomonas reinhardtii*. We have designed low-cost earth-abundant crystalline silicon (cSi)-based single-junction thin-film PV solar cells utilizing the MTHN structure. The proposed structure shows absorption characteristics insensitive to the incident light's polarization, and an optimized MTHN structure's light absorption efficiency (LAE) is 94%. We calculated the power conversion efficiency (η_{PCE}) with different nanopillar heights (h_{np}) to analyze the effect on optical and electrical performances. We also investigated the impact of bulk doping concentration (p) on the open circuit voltage (V_{oc}), short circuit current density (J_{sc}), and η_{PCE}. The value of η_{PCE} reaches 16.14% using the MTHN structure, which is the maximum value for cSi-based single-junction thin-film PV solar cells in the wavelength range of 400 to 1000 nm.

1. Introduction

Solar energy is an essential renewable source for sustainable development with zero carbon footprint [1–3]. The total available solar power on earth's surface is ~9×10^4 TW/year, much greater than the current global demand of ~15–18 TW/year [4,5]. Solar power is being explored in several technologies, e.g., photovoltaic (PV), photocatalysis, and solar-thermal [6–9]. The PV technology is the most efficient and practical way of converting solar energy into electricity [2,10]. The performance of a PV solar cell crucially depends on photo-absorbing materials and structures [11–13]. PV solar cells must be low-cost, highly efficient, and durable for widespread deployment [2,14]. Hence, low-cost earth-abundant photo-absorbing materials and efficient structures are required for faster adoption of PV solar cells [15,16].

The structural features of the photo-absorbing layer in a PV solar cell are crucial for capturing the incident sunlight. The photo-absorbing layer must absorb the available solar energy and convert it into electricity efficiently [17,18]. In the last two decades, many photo-absorbing structures have been designed to meet the required criteria of PV solar cells [19–24]. Nanophotonics-based structures and perovskite solar cells are promising options for effective light absorption. Perovskite solar cells are outstanding in enhancing light absorption. However, their widespread deployment is limited due to instability, the toxicity of materials, and the degradation of electrical performances at the junctions [25,26]. On the other hand, nanophotonic photo-absorbing structures developed by advanced fabrication techniques exhibit broadband light absorption with low-cost materials [27,28]. Nanophotonic photo-absorbing structure designs have also been bioinspired, utilizing light absorption functions in natural creatures [28,29].

Nature has many micro and nanostructures in insects and plants, e.g., flowers, moths, beetles, fireflies, butterflies, and cyanobacteria, with exceptional optical properties [30,31]. The divergent flower *Tagetes erecta* L. exhibits excellent light harvesting and antireflective properties due to a quasi-spherical symmetrical structure [32]. Multilayer structures in fireflies enhance light absorption by manipulating multiple photons [32,33]. The butterfly wings exhibit extraordinary optical behavior due to the diffraction in grating and nanophotonic crystals [32–34]. The most interesting biological structure is moth eyeballs, which consist of multi-scale microdomes with well-ordered nanostructures. Inspired by the moth eyeball structure, many researchers have developed advanced geometries, e.g., nanorods, pyramids, microlenses, and inverted cones, to enhance light absorption and reduce optical losses [32,34].

Recently, researchers have drawn much attention to enhancing light absorption by utilizing cyanobacteria's structures and light-harvesting

* Corresponding author.
E-mail address: anis@eee.buet.ac.bd (M.A. Talukder).

https://doi.org/10.1016/j.solener.2024.112777
Received 25 April 2024; Received in revised form 10 July 2024; Accepted 12 July 2024
Available online 5 August 2024

functionality [35]. Notably, Cyanobacteria exhibits nearly perfect light absorption, emerging as one of the most mesmerizing parts of the bioinspired PV solar cell [35]. *Chlamydomonas reinhardtii* is a single-cell green algae cyanobacterium with outstanding light-absorption efficiency (LAE) in both high- and low-light environments [36,37]. *Chlamydomonas reinhardtii* structure comprises different monomers and trimers, consisting of a pair of core protein complexes [38,39]. The monomer has circular-shaped proteins, whereas the trimer consists of three elliptical-shaped proteins. The presence of multiple monomers and trimers creates significant structural heterogeneity in *Chlamydomonas reinhardtii*, resulting in a remarkable improvement of light absorption [38]. Therefore, a new array of monomer and trimer-based heterogeneous nanopillar (MTHN) structures can be used for efficient light absorption in PV solar cells utilizing shape and heterogeneous functionality inspired by *Chlamydomonas reinhardtii*.

Thin-film inorganic solar cells are efficient regardless of needing much less material [40,41]. In present fabrication technological trends, manufacturing thin-film solar cells is not complex. The thickness of thin-film solar cells is several nanometers to 10 μm, much smaller than the conventional first-generation crystalline silicon (cSi) solar cells [11,40]. cSi-based thin-film solar cells are a promising option for designing efficient and low-cost PV solar cells [41,42]. In addition, a single absorbing material offers faster carrier transport, lower carrier recombination rate, and increased power conversion efficiency (η_{PCE}) [43]. Several research works have reported η_{PCE} up to 14% for cSi-based thin-film solar cells utilizing nanophotonic structures [24,40,44,45]. The thin film of amorphous-Si/nanocrystalline-Si multi-junction solar cells shows η_{PCE} of ~10%–14% using an anti-reflective coating or nanophotonic-based design [46,47]. Xue et al. developed a cSi-based thin-film PV solar cell using inverted-pyramid nanostructures with 12% efficiency [24]. Polycrystalline silicon-based thin-film solar cells with glass textures have shown η_{PCE} of 10%–12%, combining the advantages of standard silicon wafer-based technology, durability, and good electronic properties [48]. Sonntag et al. obtained η_{PCE} of 13.2% using a liquid phase crystallized silicon on glass with a thickness of 13 μm to reduce material cost, series resistance, and bulk recombination [49].

In this work, we propose cSi-based single-junction thin-film (SJTF) solar cells utilizing the MTHN structure inspired by *Chlamydomonas reinhardtii* for improved performance. Firstly, we determine the optimized parameters of the MTHN structure for efficient light absorption using the finite-difference time-domain (FDTD) method. We analyze the sensitivity of the proposed MTHN structure to the transverse electric (TE) and magnetic (TM)-polarized incident light. The optimized MTHN structure shows a polarization-insensitive high LAE of 94%. The elliptical-shaped trimer and circular-shaped monomer nanopillars, along with their heterogeneous functionality within the proposed MTHN structure, significantly enhance light absorption for both TE- and TM-polarized incident light in cSi-based nanophotonic structures from shorter to longer wavelengths.

Secondly, we design cSi-based SJTF PV solar cells with indium tin oxide (ITO) top and silver (Ag) bottom contacts. Then, we perform electrical simulations using the three-dimensional (3D) finite element method (FEM) to calculate the open circuit voltage (V_{oc}), short circuit current density (J_{sc}), fill factor (FF), and η_{PCE}. We calculate η_{PCE} with different nanopillar heights to analyze the effect on electrical performances. We also investigate the impact of bulk doping concentration (p) on the device performance. Finally, we determine the maximum value of η_{PCE}, which is 16.14%, the highest for cSi-based SJTF PV solar cells considering the wavelength (λ) range of 400 to 1000 nm. The proposed cSi-based solid nanopillar structure, combined with its thin-film characteristics, leads to lower manufacturing costs, making it more commercially viable than other PV solar cells. The designed cSi-based SJTF PV solar cell can effectively convert solar energy into electricity with the highest reported η_{PCE} to date, making it a promising option for sustainable renewable energy solutions.

2. Proposed MTHN structure

Natural biological structures often provide concepts for designing new and efficient light-harvesting structures. Cyanobacteria is an antediluvian creature that effectively modulates sunlight with light-harvesting complex (LHC) proteins [50]. *Chlamydomonas reinhardtii* is a green algae cyanobacteria that contains photosystem II (PSII) organisms, consisting of a pair of core complexes surrounded by several light-harvesting complex II (LHCII) proteins [36]. Fig. 1(a) illustrates the schematic diagram of the PSII-LHCII array for *Chlamydomonas reinhardtii* parallel to the surface where the complex proteins are attached [38]. The LHCII proteins can be minor monomeric (CP26, CP29, CP43, and CP47) and major trimeric LHCIIs (S, M, and L) [38,39]. The monomeric LHCIIs have different shapes (e.g., stick, circular, and elliptical), which are less significant in light absorption. On the other hand, the trimeric LHCIIs form three identical elliptical monomers, creating a trimer shape that enhances light absorption significantly. The LHCII trimers in *Chlamydomonas reinhardtii* are distinguished as strongly ('S-trimer'), moderate ('M-trimer'), and loosely ('L-trimer') bound depending on their location and interaction with other proteins [38,51].

We propose a photo-absorbing structure inspired by *Chlamydomonas reinhardtii*, utilizing monomers, trimers, and their heterogeneity. Fig. 1(b) shows a two-dimensional (2D) cross-sectional diagram of the arrangement of monomers and trimers on the substrate of the proposed MTHN structure with 2 × 2 unit cells. The circular monomers (c-M) and elliptical trimers (e-T) create significant heterogeneity within the MTHN structure. Fig. 1(c) illustrates a 3D schematic diagram of the MTHN structure added with a thin substrate. In the xz plane of this 3D schematic, the cylindrical- and elliptical-shaped nanopillars have been arranged on the substrate in a way that makes symmetry. On the other hand, there is no symmetry in the yz plane, resulting in space heterogeneity within the MTHN structure.

The MTHN structure has different dimensional parameters critically related to the light absorption performance. The parameters h_t and h_{np} are the substrate thickness and nanopillar height, respectively, as illustrated in Fig. 1(c). Fig. 1(d) shows a unit cell in the xy plane cross-section. The parameter a is the length of the unit cell in the x and y directions, d_c is the diameter of the cylindrical-shaped nanopillar, and d_{ae} and d_{be} are the elliptical-shaped nanopillar's major and minor diameters, respectively. The relation between d_{ae} and d_{be} is $d_{be} = d_{ae}(\sqrt{1-e^2})$, where e is the eccentricity. We have kept e fixed at 0.72 to maintain the elliptical shapes identical to *Chlamydomonas reinhardtii*. The distance between two consecutive trimers is the pitch (P). The free space within an e-T is controlled by the diameter (d_{in}) of an inner circle (red dashed circle). The diameter d_{in} is related to d_{be} as $d_{in} = d_{be} \times S_{in}$, where S_{in} is a factor.

3. Optical simulation

We perform optical simulation using the 3D FDTD method in the MIT Electromagnetic Equation Propagation (MEEP) software [52]. We use air in the simulation domain in the MEEP software while constructing the proposed MTHN structure. The MTHN structure is periodic in the x- and y-directions, whereas a perfectly matched layer (PML) boundary has been set up in the z-direction for simulation purposes. We use a Gaussian pulse as the incident light source, having a spectrum from 400 to 1000 nm and comprising >85% of the available solar energy. cSi is used as the photo-absorbing material in the MTHN structure. We consider both TE- and TM-polarized incident light to find the proposed MTHN structure's optimum parameters for polarization-insensitive absorption characteristics. We vary geometric parameters to optimize the MTHN structure and comprehensively investigate the absorption spectrum, $A(\lambda)$, and LAE. $A(\lambda)$ is calculated from the transmittance, $T(\lambda)$ and reflectance spectra, $R(\lambda)$ as

$$A(\lambda) = 1 - T(\lambda) - R(\lambda). \quad (1)$$

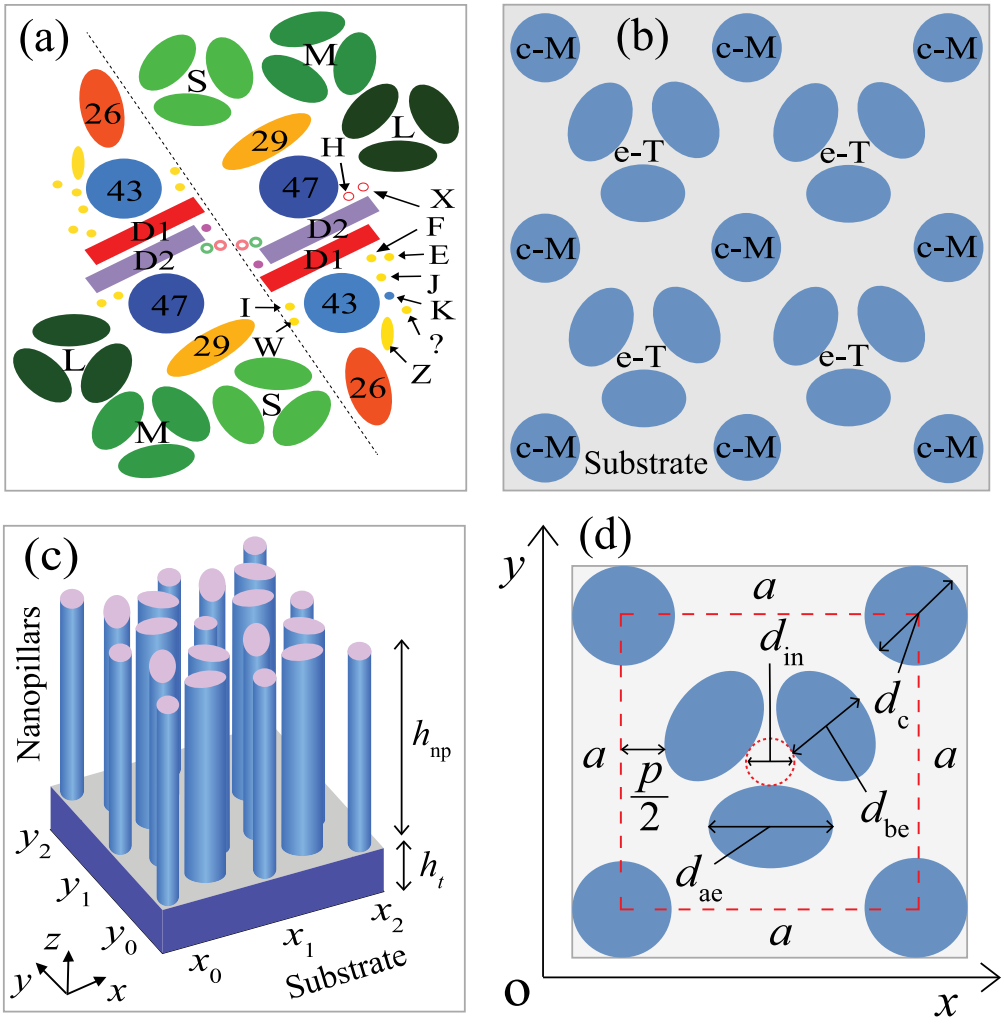

Fig. 1. (a) Schematic diagram of PSII–LHCII array for *Chlamydomonas reinhardtii* parallel to the top surface of the substrate where the complex proteins are attached. (b) The proposed arrangement of circular monomers (c-M) and elliptical trimers (e-T) on the substrate with 2 × 2 unit cells. (c) 3D schematic diagram of the proposed MTHN structure with the substrate. The material is p-type cSi. (d) A unit cell of the proposed MTHN structure (red dashed square).

Table 1
Initial values of the proposed MTHN structure's dimensional parameters for optical simulation.

Structure parameter	Value	Structure parameter	Value
e	0.72	S_{in}	0.7
d_c	150 nm	P	100 nm
h_{np}	5.0 μm	h_t	1.5 μm

LAE is calculated by the ratio between the absorbed and incident photon energies, written as

$$\mathrm{LAE} = \frac{\int (\lambda/hc) A(\lambda) I(\lambda)\, d\lambda}{\int (\lambda/hc) I(\lambda)\, d\lambda}, \tag{2}$$

where $I(\lambda)$ is the incident source spectrum, h is the Planck constant, and c is the speed of light. We calculate LAE considering wavelengths from 400 nm to 1000 nm.

3.1. Optimized MTHN structure

Cylindrical-shaped nanopillars enhance light absorption with broadband characteristics and create heterogeneity within the MTHN structure, resembling the functionality of *Chlamydomonas reinhardtii*. Additionally, they can be represented as minor circular-shaped monomers that show monomeric intrinsic properties of *Chlamydomonas reinhardtii*. They increase the surface area for enhanced photon interactions. The internal reflections between the monomer and trimer depend on the free space between them. To find the appropriate free space and shape for cylindrical nanopillar, we vary d_c from 80 to 150 nm, and the corresponding results of $A(\lambda)$ and LAE are given in Fig. 2(a). When d_c increases, the free space decreases, creating insufficient space for light interaction and coupling. On the other hand, a smaller d_c makes a larger free space, causing higher scattering losses. Therefore, d_c = 110 nm provides an appropriate free space within the MTHN structure for maximum $A(\lambda)$ and LAE. In particular, it increases broadband light absorption to >90% for $\lambda \lesssim 900$ nm.

The free space between the trimer and monomer also depends on P, which determines the distance between two consecutive unit cells in the xy plane. Fig. 2(b) shows the effects of P on $A(\lambda)$ and LAE. The LAE is maximum when P = 100 nm. However, LAE decreases for P > 100 nm due to increased free space, and likewise, LAE decreases for P < 100 nm due to a lower light absorption within the smaller free space. Therefore, the optimum P is at 100 nm based on the maximum LAE and $A(\lambda)$ results. However, $A(\lambda)$ still needs to be improved in the longer wavelength range of >900 nm.

The elliptical-shaped trimers of the MTHN structure primarily contribute to the modulation of photons by the surface area of nanopillars and the free space within them, resulting in significant light absorption. The parameters d_{ae} and S_{in} determine trimer shapes, affecting the effective absorption surface area and free space within the trimer. Initially,

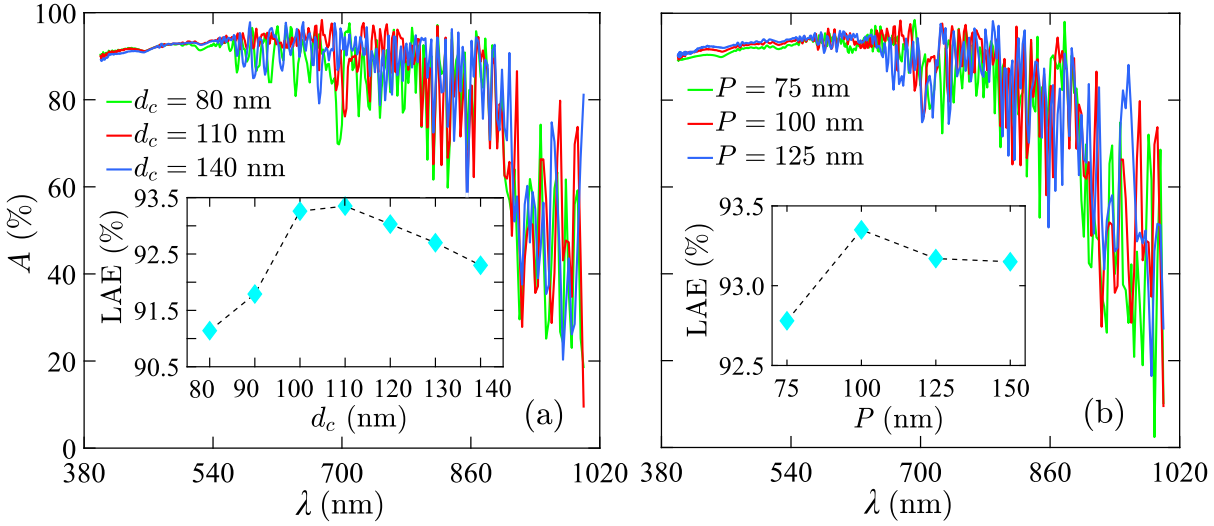

Fig. 2. $A(\lambda)$ and LAE (inset) with different (a) d_c and (b) P.

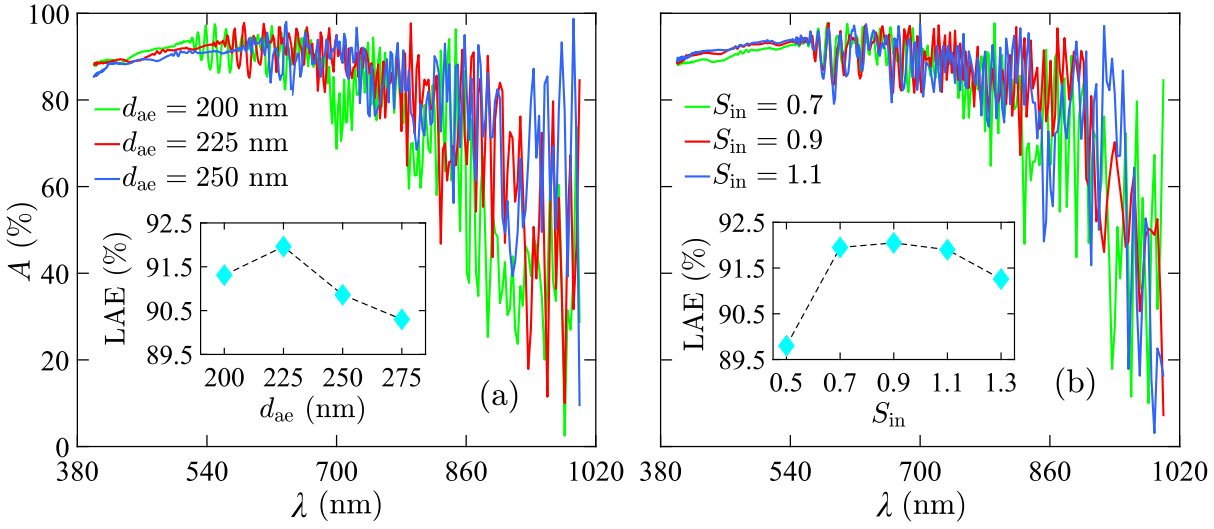

Fig. 3. $A(\lambda)$ and LAE (inset) with different (a) d_{ae} and (b) S_{in}.

we vary d_{ae} from 200 to 275 nm to find the optimized elliptical-shaped nanopillars, keeping other parameters constant, as given in Table 1. Fig. 3(a) shows $A(\lambda)$ for different d_{ae} with LAE given in the inset plot. Varying d_{ae} has less significant changes in $A(\lambda)$ at the shorter wavelengths. However, $A(\lambda)$ improved in the longer wavelengths for more promising resonant absorption. The structure shows maximum LAE and $A(\lambda)$ with $d_{ae} = 225$ nm.

The distance between two elliptical nanopillars within a trimer is related to S_{in}, with $S_{in} < 0.5$ resulting in overlapping elliptical nanopillars. Therefore, we vary S_{in} from 0.5 to 1.3. Fig. 3(b) shows the effects of S_{in} on $A(\lambda)$ and LAE. A smaller value of S_{in} makes a smaller free space within the trimer, resulting in a higher reflectance. On the other hand, a greater S_{in} results in higher transmittance due to larger free space within the trimer. Therefore, $A(\lambda)$ and LAE decrease at the higher and the lower values of S_{in}. LAE and $A(\lambda)$ are maximum when $S_{in} = 0.9$. Nevertheless, $A(\lambda)$ is not improved at the longer wavelengths as expected.

The nanopillar height (h_{np}) is a crucial parameter to modulate effective optical absorption by controlling the light-coupling surface area. Nanopillars help to reduce reflection losses due to multiple internal reflections, enhancing resonant absorption. We vary h_{np} to find its optimum value in the MTHN structure, and the corresponding results of $A(\lambda)$ and LAE are shown in Fig. 4(a). As h_{np} increases from 2.5 to 10 μm, LAE improves by 3% due to enhanced surface area with the higher h_{np} and significant improvement of $A(\lambda)$ at longer wavelengths. The increased depth of the cavity due to the higher h_{np} results in more photon interactions and localization for efficient light absorption. The localization of photons occurs through various optical mechanisms associated with nanostructures. These mechanisms include multiple internal reflection phenomena, discrete multi-resonant modes, and Mie-type resonances [53–55]. The internal reflection of incident light within optimal inter-nanopillar gaps and the optical path length, which depends on the nanopillar height, enhances the probability of photon reabsorption by the trapped incoming photons within the proposed MTHN structure. The various shapes of the nanopillars create multi-resonant modes within the cavity, allowing them to localize and interact with more photons. In addition, the incident light interacts with the nanopillars and substrate of the proposed solar cell structure, creating Mie-type resonances that significantly enhance photon absorption within the structure. This enhanced light absorption generates more charge carriers, leading to the efficient conversion of solar energy into electricity. However, the improvement of LAE is minimal for $h_{np} >$ 10 μm. Therefore, we choose $h_{np} = 10$ μm as an optimum value, which ensures reduced material cost, rapid charge carrier transportation, and lower charge carrier recombination in PV solar cells.

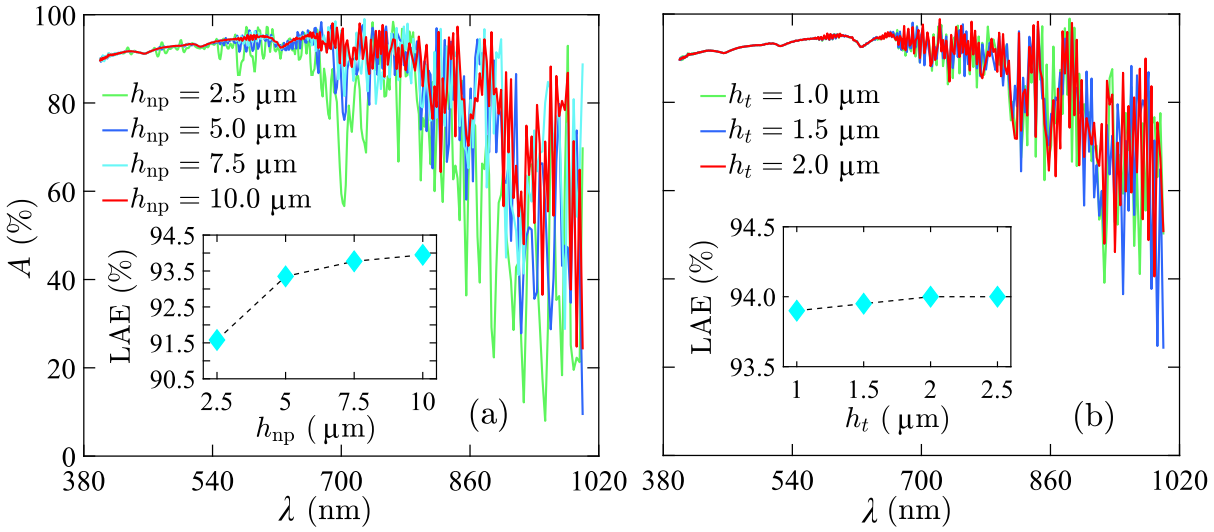

Fig. 4. $A(\lambda)$ and LAE (inset) with different (a) h_{np} and (b) h_t.

Table 2
The optimum value of the parameters for the optimized MTHN structure.

Structure parameter	Optimum value	Structure parameter	Optimum value
d_{ae}	225 nm	S_{in}	0.90
d_c	110 nm	P	100 nm
h_{np}	10.0 μm	h_t	2.0 μm

The base of the nanopillars is the substrate, having a minor role in light absorption of the MTHN structure. Fig. 4(b) shows the effects of h_t on $A(\lambda)$ and LAE. The improvement of $A(\lambda)$ and LAE is approximately negligible for $h_t > 2.0$ μm. Therefore, we take $h_t = 2.0$ μm as the optimum substrate thickness, considering additional concerns to reduce back-scattering in PV solar cells. Specifically, the optimum $h_t = 2$ μm is a good basis for the mechanical strength of standing nanopillars. Noticeably, the absorbance spectrum shows various discrete resonance modes at longer wavelengths, depending on the diameter of nanopillars and their structural periodicity [56]. The dominant resonance peaks are attributed to the Mie resonance effect, while the weak ones originate from light scattering losses and the Wood-Rayleigh anomaly effect [55,57,58]. Finally, $A(\lambda)$ is improved as expected at the longer wavelengths above 900 nm for the optimized MTHN structure.

Table 2 shows the obtained optimum structure parameter values. The maximum LAE is 94% for the optimized MTHN structure, and the maximum achievable photocurrent density (J_{MAPD}) is 32.30 mA cm^{-2} determined by

$$J_{MAPD} = \int \frac{e\lambda}{hc} A(\lambda)\phi_{AM1.5G}(\lambda)\, d\lambda, \tag{3}$$

where $\phi_{AM1.5G}(\lambda)$ is the solar incident light of the AM1.5G spectrum [59]. J_{MAPD} is regarded as the ideal short circuit current density (J_{sc}) without considering surface and bulk recombination, i.e., each absorbed photon produces an electron–hole pair.

3.2. Polarization-insensitive light absorption

Sunlight is an electromagnetic wave propagating with random polarizations due to photon scattering by atmospheric medium. Hence, designing a polarization-insensitive photo-absorbing structure for efficient PV solar cells is essential. Fig. 5(a) shows $A(\lambda)$ and LAE with TE- and TM-polarized incident light for the MTHN structure. $A(\lambda)$ is the same for TE- and TM-polarized light at shorter wavelengths up to 700 nm. However, the resonance peak positions vary in the longer wavelengths, although the light absorption shows a similar trend. The LAE is almost the same for TE- and TM-polarized incident light, resulting in polarization-insensitive absorption characteristics for the MTHN structure.

Fig. 5(b)–(e) depict the electric field profiles for TE- and TM-polarized light with different wavelengths on the xy plane of the MTHN structure at the interface of nanopillars and substrate. At $\lambda = 505$ nm, strong light interactions and coupling are present in the free space within the MTHN structure due to multiple internal reflections on the side-wall surface of nanopillars, as shown in Fig. 5(b) and (d) for TE- and TM-polarized light, respectively. On the other hand, effective light absorption occurs in nanopillars at $\lambda = 805$ nm, as illustrated in Fig. 5(c) and (e) for TE- and TM-polarized light, respectively. Specifically, the elliptical nanopillars absorb the maximum portion of solar energy. Moreover, the heterogeneity of monomers and trimers helps effective light absorption from the shorter to the longer wavelengths. The integrated spatial electric field intensity for TE- and TM-polarized light is approximately the same to evince the polarization-insensitive characteristics and effective light absorption. Also, the spatial electric field confirms the heterogeneity within the MTHN structure at different λ, demonstrating the successful implementation of light absorption mechanism in *Chlamydomonas reinhardtii*.

3.3. Effects of bottom and top contacts

The bottom (BC) and the top contacts (TC) are essential integrated parts for charge carrier transportation in PV solar cells. They are usually metal elements and can impact on the optical light absorption. Here, we use a 150-nm thick (h_{bc}) silver (Ag) BC in the MTHN structure. Ag offers good electrical conductivity, low resistance, and an ohmic contact with p-type silicon semiconductors [60,61]. Ag BC also works as a back reflector (BR) and contributes to reducing transmittance losses. Fig. 6(a) shows the BC's effects on $A(\lambda)$, $T(\lambda)$, and LAE. Notably, $T(\lambda)$ reduces to zero due to reflection from BC. The scattering of photons at the interface between the BC and the substrate increases the photons' path lengths within the structure, enhancing the probability of absorption. Reusing the scattered photons contributes to producing more electron–hole pairs, and some photons get reabsorbed effectively due to the minimum photon energy ($\lambda \leq 1000$ nm) being higher than the bandgap energy of Si ($\lambda \leq 1107$ nm). As a result, $A(\lambda)$ improves at longer wavelengths with the BC. Even if the light absorption is enhanced, LAE increases barely due to the smaller photon energy in the longer wavelengths.

On the other hand, the TC acts as an emitter and is placed on the top of nanopillars in the MTHN structure. The TC can affect light absorption

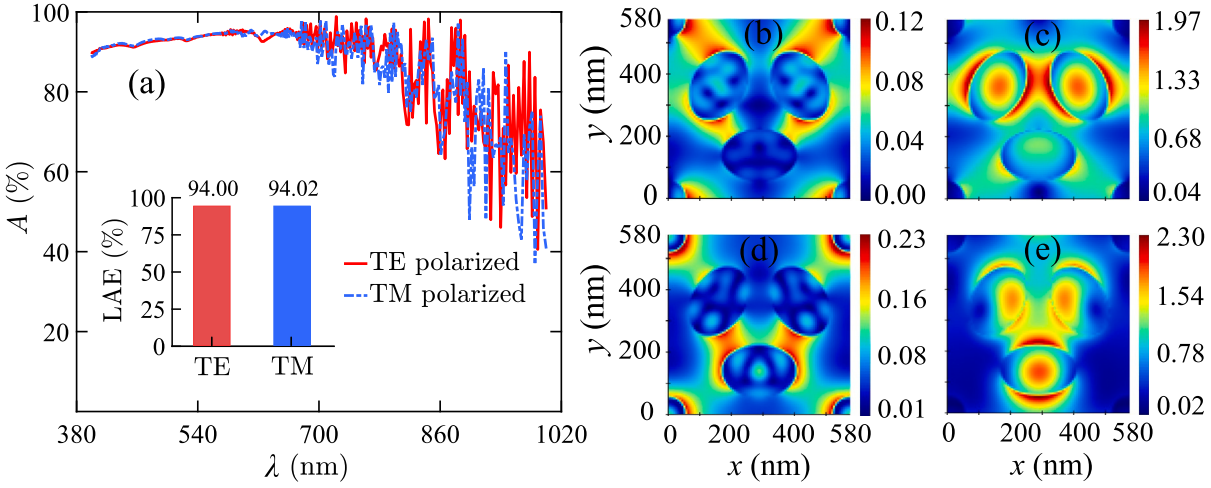

Fig. 5. (a) $A(\lambda)$ and LAE for TE- and TM-polarized light on the xy plane of the MTHN structure at the bottom of nanopillars ($z = 0$). Electric field distribution for TE-polarized light at (b) $\lambda = 505$ nm and (c) $\lambda = 805$ nm and TM-polarized light at (d) $\lambda = 505$ nm and (e) $\lambda = 805$ nm.

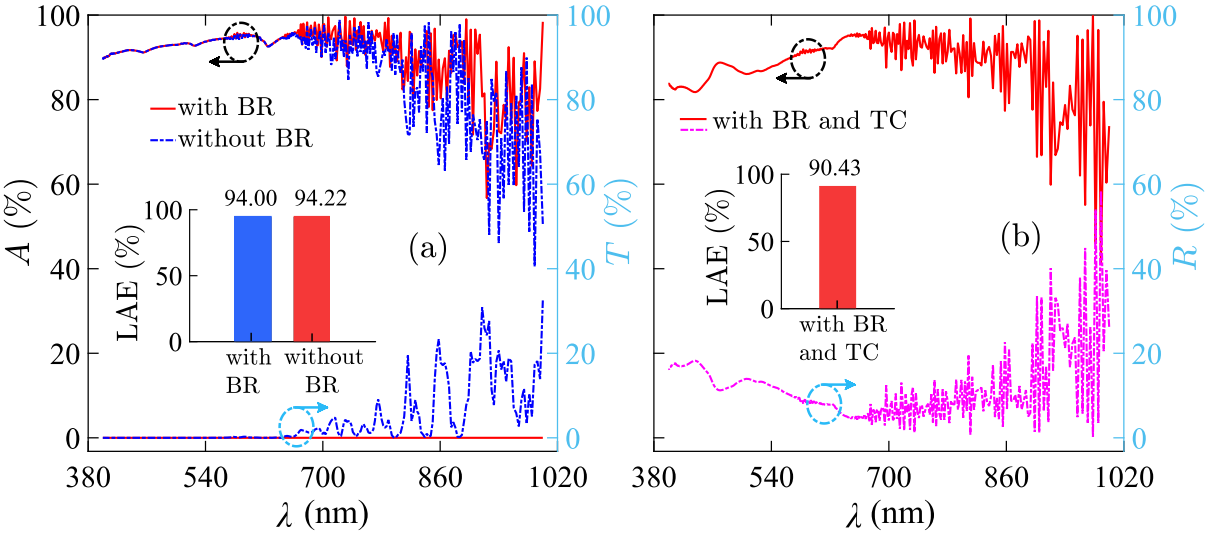

Fig. 6. (a) $A(\lambda)$, $T(\lambda)$, and LAE with a back-reflector (BR) as silver (Ag) and without the BR. (b) $A(\lambda)$, $R(\lambda)$, and LAE with both the BR and a top contact (TC) as indium tin oxide (ITO).

if it has high reflectance and poor transparency. It is essential to use a conductive metal as the TC that is also highly transparent and negligibly reflective. This work uses an ITO layer as the TC, which is highly transparent to sunlight and electrically conductive. The thickness of the ITO layer (h_{tc}) is 150 nm, providing the required transparency and conductivity. Fig. 6(b) shows the effect of using the BC and the TC on $A(\lambda)$, $R(\lambda)$, and LAE. $A(\lambda)$ is nearly the same in the longer wavelengths. However, it decreases by 5%–7% in shorter wavelengths due to increased reflection and scattering losses by the TC. $R(\lambda)$ is $< 10\%$ at $\lambda \sim 520$–920 nm, whereas it is $< 20\%$ at $\lambda \lesssim 520$, and increases up to 40% at $\lambda \gtrsim 920$. Eventually, the conclusive optical outcomes of LAE is receded to 90.43% for the optimized MTHN structure because of considering the TC and corresponding J_{MAPD} is 32.57 mA cm^{-2}.

4. Electrical simulation

4.1. Simulation model and specification

Electrical simulations are critical to determine how efficiently the PV solar cells convert absorbed solar energy into electrical energy. The fundamental outcomes of the simulation are J vs. V and J vs. P characteristics, where J, V, and P are the current density, voltage, and electrical power, respectively. From a practical point of view, this simulation is an essential step for calculating PV solar cells' performance as J_{MAPD} is overestimated without considering resistive and charge carrier transportation and recombination losses.

In this study, we use the coupled optoelectronic FDTD and DEVICE solvers of Lumerical to model and analyze the electrical performance of the proposed MTHN SJTF solar cell [62]. The optical simulation evaluates the electric field ($\vec{E}_{op}$) distribution within the MTHN structure using Maxwell curl equations through FDTD methods. Then, we utilize $\vec{E}_{op}$ to determine the absorbed optical power (P_{abs}) and the charge generation rate ($G(\vec{r})$). The calculation of P_{abs} incorporates $\vec{E}_{op}$ and the imaginary part of the dielectric permittivity of materials ($\Im\{\varepsilon(\vec{r},\omega)\}$) using the following equation [63]

$$P_{abs} = -\frac{1}{2}\omega\left|\vec{E}_{op}(\vec{r},\omega)\right|^2 \Im\{\varepsilon(\vec{r},\omega)\}, \tag{4}$$

where ω represents the angular frequency. Now, $G(\vec{r})$ is calculated using P_{abs} as given by [63]

$$G(\vec{r}) = \int g(\vec{r},\omega)d\omega, \tag{5a}$$

$$g(\vec{r},\omega) = \frac{P_{abs}}{\hbar\omega} = -\frac{\pi}{h}\left|\vec{E}_{op}(\vec{r},\omega)\right|^2 \Im\{\varepsilon(\vec{r},\omega)\}. \tag{5b}$$

Table 3
Electrical simulation parameters for the proposed structure.

Description of parameter	Symbol	Nominal value	Unit
Thickness of the base	h_{bc}	150	nm
Depth of the base region junction	σ_{db}	0.40	μm
Thickness of the emitter	h_{tc}	150	nm
Depth of the emitter region junction	σ_{de}	0.30	μm
Bulk doping concentration (p-type)	p	10^{16}	cm^{-3}
Acceptor concentration (base region doping)	N_A	5×10^{18}	cm^{-3}
Donor concentration (emitter region doping)	N_D	$10^{18} - 10^{19}$	cm^{-3}
Intrinsic carrier concentration at 300 K	n_i	1.5×10^{10}	cm^{-3}
Hole mobility for cSi at 300 K	μ_p	470.5	cm^2/V-s
Electron mobility for cSi at 300 K	μ_n	1471	cm^2/V-s
Hole surface recombination velocity	SRV_p	60	cm/s
Electron surface recombination velocity	SRV_n	80	cm/s
Hole SRH recombination lifetime	τ_p	4.0	μs
Electron SRH recombination lifetime	τ_n	3.3	μs
Auger recombination of holes at 300 K	C_{aup}	9.9×10^{-32}	cm^6/s
Auger recombination of electrons at 300 K	C_{aun}	2.8×10^{-31}	cm^6/s
Radiative recombination coefficient at 300 K	$C_{radiative}$	1.4×10^{-14}	cm^3/s
Incident solar irradiance power on earth	P_{in}	100	mW cm^{-3}

Then, this work solves a drift–diffusion model using Poisson, drift–diffusion, and continuity equations via a self-consistent decoupled procedure considered as the Gummel poon model [64]. The Poisson, drift–diffusion, and continuity equations are written by [65]

$$-\nabla \cdot (\varepsilon_{dc} \nabla V) = e\rho_c, \tag{6a}$$

$$\overrightarrow{J_n} = e\mu_n n\overrightarrow{E} + eD_n \nabla n, \tag{6b}$$

$$\overrightarrow{J_p} = e\mu_p p\overrightarrow{E} - eD_p \nabla p, \tag{6c}$$

$$\frac{\partial n}{\partial t} = \frac{1}{e}\nabla \cdot \overrightarrow{J_n} - R_n, \tag{6d}$$

$$\frac{\partial p}{\partial t} = -\frac{1}{e}\nabla \cdot \overrightarrow{J_p} - R_p, \tag{6e}$$

$$D_n = \frac{\mu_n k_B T}{e}, \tag{6f}$$

$$D_p = \frac{\mu_p k_B T}{e}, \tag{6g}$$

where ε_{dc} is the dc dielectric permittivity, $\overrightarrow{E}$ is the electric field, ρ_c is the net charge density, $\overrightarrow{J}_{n/p}$ is the electron/hole current density, $\mu_{n/p}$ is the electron/hole mobility, $D_{n/p}$ is the electron/hole diffusivity, $R_{n/p}$ is the net charge recombination rate, k_B is the Boltzmann constant, T is the temperature, and n and p are the electron and hole densities. In order to solve the above equation, Dirichlet and Neumann boundary conditions are applied to the boundaries and interfaces of the proposed MTHN structure.

The electrical characteristics have been determined using the Gummel poon model by the 3D finite element method. This simulation considers several non-ideal effects such as the high-level injection, Shockley–Read–Hall (SRH) effect, auger, and radiative recombination losses. The bulk semiconductor is accounted as p-type with 10^{16} cm^{-3} doping concentration (p). The emitter and base regions are considered heavily doped, supporting efficient charge carrier injection. ITO and Ag are used as the emitter and the base, respectively. The work function of ITO is ≈4.2–4.5 eV for the PV solar cell, and the electrical conductivity is ≃5000 Sm^{-2} at 150 nm thickness [66]. The solar irradiance on earth's surface is considered as input power (P_{in}), whose average value is approximately 100 mW cm^{-2}. The parameters used in the electrical simulation model are presented in Table 3.

Table 4
FF with varying p for different h_{np}, where $N_A = 5 \times 10^{18}$ and $N_D = 2 \times 10^{18}$ cm^{-3}.

p	FF (%)		
(cm^{-3})	h_{np} = 5.0 μm	h_{np} = 7.5 μm	h_{np} = 10 μm
10^{14}	75.20	75.21	75.25
10^{15}	77.90	77.98	77.99
10^{16}	83.11	83.20	83.20

4.2. J-V and P-V characteristics with power conversion efficiency

The key performance parameters for PV solar cells are J, V, P, and η_{PCE}. Fig. 7 depicts the performance parameters for cSi-based SJTF PV solar cells utilizing the proposed MTHN structure with h_{np} = 5.0, 7.5, and 10 μm. We vary h_{np} to investigate its impact on electrical performances since charge carrier mean-free path and lifetime will depend on h_{np}. Fig. 7(a) and (b) depict the J vs. V and P vs. V characteristics with different h_{np}, respectively. Varying h_{np} from 5.0 to 10 μm affect an increase in J_{sc} for more light absorption and consequently decreasing V_{oc} due to inverse relationship with J_{sc}. The J_{sc} results for h_{np} values of 5 and 10 μm are 29.98 and 30.61 mA cm^{-2}, respectively. The corresponding V_{oc} values are 0.642 V and 0.634 V under the same conditions. When h_{np} is 10 μm, the maximum obtained P_{out} is 16.14 mW cm^{-2} with an operating voltage (V_{op}) and current density (J_{op}) of 0.55 V and 29.35 mA cm^{-2}, respectively. Decreasing the value of h_{np} results in lower P_{out} and J_{op}, but slightly increases V_{op}. Therefore, the effects of h_{np} variations on J-V and P-V characteristics are insignificant since the electron and hole diffusion lengths of Si (100–300 μm) are much greater than the dimensions of h_{np} considered in this work.

Fig. 7(c) and (d) show η_{PCE} and FF with different h_{np}, respectively. η_{PCE} and FF are calculated from J–V and P–V characteristics as

$$\eta_{PCE} = \frac{P_{out}}{P_{in}}, \tag{7a}$$

$$FF = \frac{\eta_{PCE} \times P_{in}}{J_{sc} \times V_{oc}} = \frac{P_{out}}{J_{sc} \times V_{oc}}. \tag{7b}$$

For h_{np} = 10 μm, η_{PCE} reaches maximum value by 16.14%, which is the highest value of a single junction cSi-based thin-film PV solar cells utilizing simply solid nanopillar structure. η_{PCE} varies slightly with different h_{np} due to their light absorption being approximately the same up to λ = 900 nm, i.e., charge generations are nearly the same. For PV solar cells, FF depends on the resistive parameter in the electrical model, e.g., top and bottom contact, bulk, base, and emitter region resistance. Therefore, FF is the same with different h_{np} for considering the identical doping concentration, the base, and the emitter.

4.3. Effects of doping concentration

The performance of PV solar cells depends on the bulk doping concentration (p) [67,68]. Fig. 8(a) shows J_{sc} and V_{oc} varying with p for different h_{np}. The calculated J_{sc} is maximum at h_{np} = 10 μm. J_{sc} is greater for smaller p due to a wider depletion region, which is beneficial for fast carrier separation and collection. On the other hand, a greater p makes deep coulomb traps, which reduces carrier mobility, resulting in a smaller J_{sc}. V_{oc} follows the same trend of J_{sc} for different p. However, V_{oc} reaches the maximum at h_{hp} = 5.0 μm due to the shorter charge carrier path and smaller resistive losses.

Fig. 8(b) shows η_{PCE} vs. p for different h_{np}. The maximum η_{PCE} has been achieved with $p = 10^{16}$ cm^{-3} for each h_{np}. Although J_{sc} and V_{oc} are greater at $p = 10^{14}$ cm^{-3}, η_{PCE} decreases ~1.25–1.30% due to smaller FF. Table 4 shows that FF critically depends on the majority carrier concentration of p with an inverse relationship. As a result, FF decreases ~8% for $p = 10^{14}$ cm^{-3} compared to $p = 10^{16}$ cm^{-3}. On the other hand, $p \gtrsim 10^{16}$ cm^{-3} is undesirable for the damage of crystal structure within the bulk material and extensive costs [69,70]. Therefore, the optimum

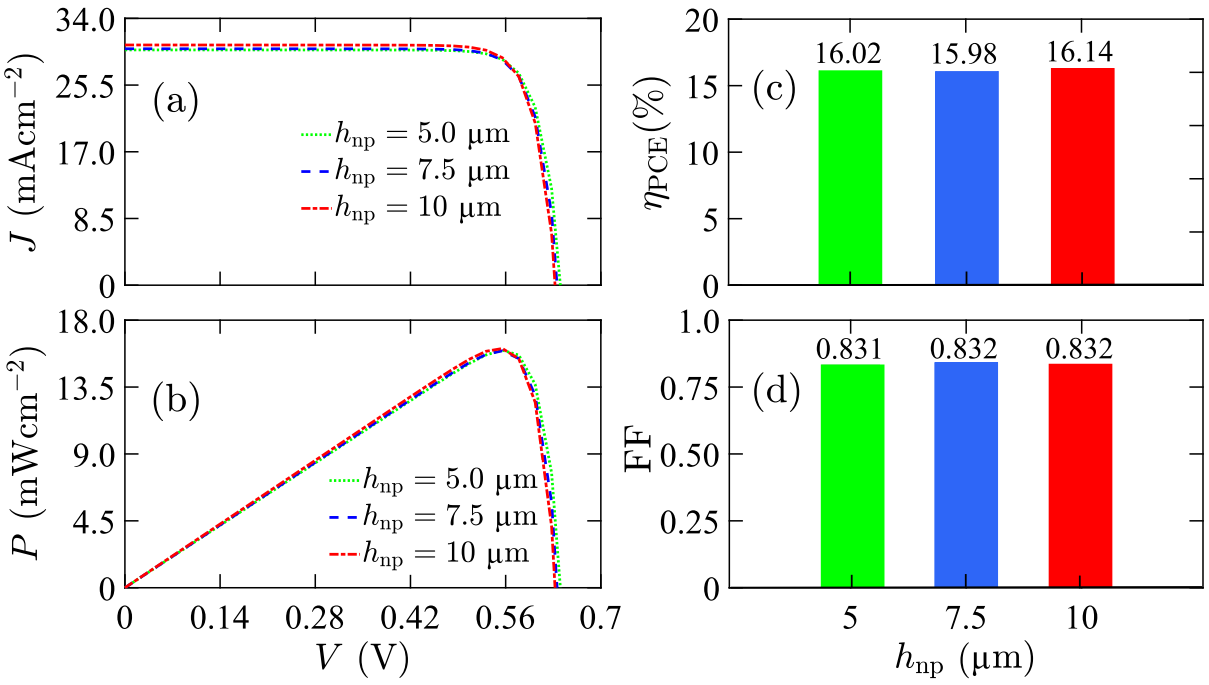

Fig. 7. (a) J–V characteristics, (b) P–V characteristics, (c) η_{PCE}, and (d) FF for the single junction cSi-based thin-film PV solar cell utilizing the MTHN structure with different h_{np}.

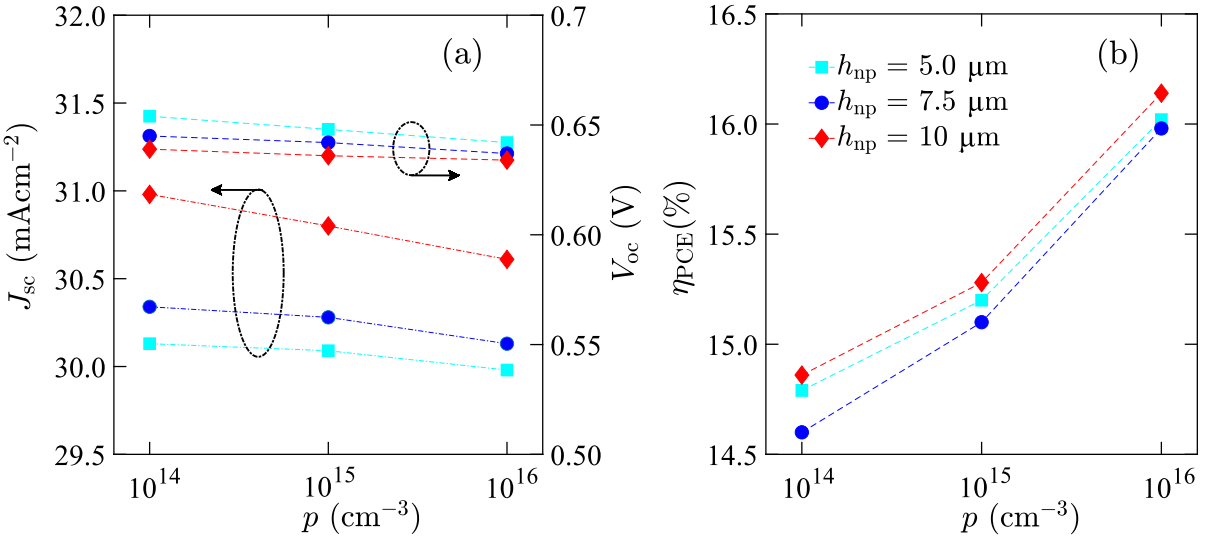

Fig. 8. (a) Effects of p on J_{sc} and V_{oc} with different h_{np}, where symbols ■, ●, and ◆ indicate h_{np} = 5.0, 7.5, and 10 μm, respectively. (b) Effects of p on η_{PCE} with different h_{np}.

p is 10^{16} cm^{-3} in this work. Finally, we vary $N_D = 10^{18}$–10^{19} cm^{-3} to keep $N_A = 5 \times 10^{18}$ cm^{-3} to observe the effects of the emitter region doping concentration. The variation of N_D in the range has a negligible impact on the performance of the PV solar cells.

In order to compare the electrical performance of the MTHN SJTF solar cell without taking the MTHN structure into account, we simulated a planar 12 μm thin-film silicon solar cell and calculated its electrical characteristics. Fig. 9 compares the planar and MTHN SJTF solar cells in their performances of J_{sc} and η_{PCE}, considering different values of p. Increasing p does not significantly impact J_{sc} but improves η_{PCE} by ~1.5% for both cases. The MTHN SJTF solar cell shows approximately twice J_{sc} and η_{PCE} than the planar thin-film solar cell. In addition, detailed comparisons of various thin-film solar cell structures from existing literature with the proposed MTHN solar cell are presented in Table 5.

Table 5
Comparison of electrical performances of the proposed MTHN SJTF solar cell with those in existing literature.

PV solar cells	J_{sc} (mA cm^{-2})	η_{PCE} (%)	Ref.
Si nano-wire	27.5	7.53	[71]
Si nano-pencils	28.5	8.7	[72]
cSi nanopillars	36.89	14.83	[73]
Ultra-thin cSi NS	23.7	12.3	[24]
a-Si:H (thin film)	16.36	10.2	[74]
c-Si:H (thin film)	29.72	11.9	[74]
Si (TF mini-module)	29.7	10.5	[75]
cSi nano-honeycomb	30	11.0	[76]
cSi thin film (12 μm)	17.71	8.65	This work
MTHN SJTF solar cells	30.61	16.14	This work

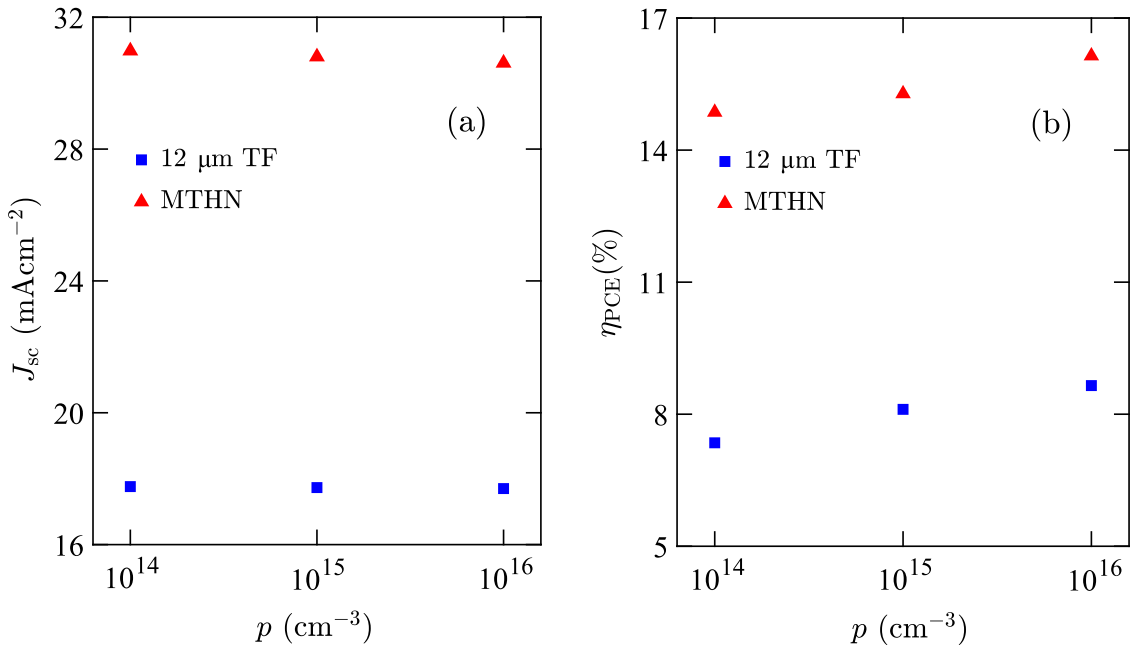

Fig. 9. Comparison between a planner structure of 12 μm thin-film and MTHN SJTF cSi solar cells of (a) J_{sc} and (b) η_{PCE} considering different values of p.

Recently, cSi solar cells with inverted-pyramid nanostructures and a flexible, free-standing 2.7 μm-thick ultra-thin film achieved an efficiency of 12.3% experimentally [24]. In contrast, an efficiency of 14.83% was demonstrated using optimized silicon nanopillars with an average diameter of 600 nm and height of 1.5 μm [73]. These results are close to the simulated efficiency of MTHN SJTF solar cells, suggesting the possibility of experimentally achieving this work's promising result. Additionally, this work shows that SJTF solar cells not only reduce material costs but also produce maximum output power by employing the novel MTHN structure inspired by *Chlamydomonas reinhardtii*.

5. Conclusion

In summary, we proposed a single junction cSi-based thin-film PV solar cell utilizing the MTHN structure inspired by *Chlamydomonas reinhardtii*. The optical performance is obtained with an outstanding LAE of 94% for both TE- and TM-polarized light for the optimized MTHN structure, showing enhanced light absorption capability irrespective of the incident light's polarization. We exploited the heterogeneity within the MTHN structure for enhanced light absorption, coupling intense electric field intensity between the nanopillars. The resulting J_{sc} and V_{oc} of the proposed MTHN SJTF solar cell are 30.61 mA cm^{-2} and 0.634 V, respectively, considering h_{np} = 10 μm. The calculated maximum η_{PCE} is 16.14% with FF = 83.2%, the highest for a cSi-based SJTF PV solar cell utilizing only a solid nanopillar structure. The calculated η_{PCE} does not vary much with nanopillar dimensions. However, η_{PCE} increases by ~1.5% when p changes from 10^{14} to 10^{16} cm^{-3}. Therefore, the proposed MTHN structure-based cSi SJTF PV solar cell can contribute to efficiently converting solar energy into electrical power for practical realization and widespread deployment.

CRediT authorship contribution statement

Abdul Ahad Mamun: Writing – original draft, Validation, Methodology, Formal analysis, Conceptualization. **Jawadul Karim:** Writing – original draft, Validation, Software, Formal analysis. **Muhammad Anisuzzaman Talukder:** Writing – review & editing, Supervision, Methodology.

Declaration of competing interest

The authors declare that they have no known competing financial interests or personal relationships that could have appeared to influence the work reported in this paper.

References

[1] J. Yu, Y.M. Tang, K.Y. Chau, R. Nazar, S. Ali, W. Iqbal, Role of solar-based renewable energy in mitigating CO_2 emissions: evidence from quantile-on-quantile estimation, Renew. Energy 182 (2022) 216–226.
[2] M. Victoria, N. Haegel, I.M. Peters, R. Sinton, A. Jäger-Waldau, C. del Canizo, C. Breyer, M. Stocks, A. Blakers, I. Kaizuka, et al., Solar photovoltaics is ready to power a sustainable future, Joule 5 (5) (2021) 1041–1056.
[3] A.O. Maka, J.M. Alabid, Solar energy technology and its roles in sustainable development, Clean Energy 6 (3) (2022) 476–483.
[4] A.R. Fareza, F.A.A. Nugroho, F.F. Abdi, V. Fauzia, Nanoscale metal oxides–2D materials heterostructures for photoelectrochemical water splitting—a review, J. Mater. Chem. A 10 (16) (2022) 8656–8686.
[5] L. Jin, H. Zhao, Z.M. Wang, F. Rosei, Quantum dots-based photoelectrochemical hydrogen evolution from water splitting, Adv. Energy Mater. 11 (12) (2021) 2003233.
[6] M. Okil, M. Salem, T.M. Abdolkader, A. Shaker, From crystalline to low-cost silicon-based solar cells: A review, Silicon 14 (5) (2022) 1895–1911.
[7] C.S. Gopinath, N. Nalajala, A scalable and thin film approach for solar hydrogen generation: a review on enhanced photocatalytic water splitting, J. Mater. Chem. A 9 (3) (2021) 1353–1371.
[8] P. Cheng, D. Wang, P. Schaaf, A review on photothermal conversion of solar energy with nanomaterials and nanostructures: from fundamentals to applications, Adv. Sustain. Syst. 6 (9) (2022) 2200115.
[9] Y. Li, R. He, P. Han, B. Hou, S. Peng, C. Ouyang, A new concept: Volume photocatalysis for efficient H_2 generation _Using low polymeric carbon nitride as an example, Appl. Catal. B 279 (2020) 119379.
[10] P.G.V. Sampaio, M.O.A. González, Photovoltaic solar energy: Conceptual framework, Renew. Sustain. Energy Rev. 74 (2017) 590–601.
[11] B. Salhi, The photovoltaic cell based on CIGS: principles and technologies, Materials 15 (5) (2022) 1908.
[12] H. Meddeb, M. Götz-Köhler, N. Neugebohrn, U. Banik, N. Osterthun, O. Sergeev, D. Berends, C. Lattyak, K. Gehrke, M. Vehse, Tunable photovoltaics: adapting solar cell technologies to versatile applications, Adv. Energy Mater. 12 (28) (2022) 2200713.
[13] M. Fazal, S. Rubaiee, Progress of PV cell technology: Feasibility of building materials, cost, performance, and stability, Sol. Energy 258 (2023) 203–219.
[14] M. Dada, P. Popoola, Recent advances in solar photovoltaic materials and systems for energy storage applications: a review, Beni-Suef Univ. J. Basic Appl. Sci. 12 (1) (2023) 1–15.

[15] J.W. Choi, B. Shin, P. Gorai, R.L. Hoye, R. Palgrave, Emerging earth-abundant solar absorbers, 2022.

[16] P. Tawalare, Optimizing photovoltaic conversion of solar energy, AIP Adv. 11 (10) (2021).

[17] O.A. Al-Shahri, F.B. Ismail, M. Hannan, M.H. Lipu, A.Q. Al-Shetwi, R. Begum, N.F. Al-Muhsen, E. Soujeri, Solar photovoltaic energy optimization methods, challenges and issues: A comprehensive review, J. Clean. Prod. 284 (2021) 125465.

[18] G.K. Singh, Solar power generation by PV (photovoltaic) technology: A review, Energy 53 (2013) 1–13.

[19] C. Zhang, S. Wang, H. Zhang, Y. Feng, W. Tian, Y. Yan, J. Bian, Y. Wang, S. Jin, S.M. Zakeeruddin, et al., Efficient stable graphene-based perovskite solar cells with high flexibility in device assembling via modular architecture design, Energy Environ. Sci. 12 (12) (2019) 3585–3594.

[20] M. Kokkonen, P. Talebi, J. Zhou, S. Asgari, S.A. Soomro, F. Elsehrawy, J. Halme, S. Ahmad, A. Hagfeldt, S.G. Hashmi, Advanced research trends in dye-sensitized solar cells, J. Mater. Chem. A 9 (17) (2021) 10527–10545.

[21] Y.-L. He, Y. Qiu, K. Wang, F. Yuan, W.-Q. Wang, M.-J. Li, J.-Q. Guo, Perspective of concentrating solar power, Energy 198 (2020) 117373.

[22] H. Mehmood, H. Nasser, T. Tauqeer, S. Hussain, E. Ozkol, R. Turan, Simulation of an efficient silicon heterostructure solar cell concept featuring molybdenum oxide carrier-selective contact, Int. J. Energy Res. 42 (4) (2018) 1563–1579.

[23] S. Bhattacharya, S. John, Beyond 30% conversion efficiency in silicon solar cells: a numerical demonstration, Sci. Rep. 9 (1) (2019) 12482.

[24] M. Xue, K.N. Nazif, Z. Lyu, J. Jiang, C.-Y. Lu, N. Lee, K. Zang, Y. Chen, T. Zheng, T.I. Kamins, et al., Free-standing 2.7 μm thick ultrathin crystalline silicon solar cell with efficiency above 12.0%, Nano Energy 70 (2020) 104466.

[25] Y. Rong, Y. Hu, A. Mei, H. Tan, M.I. Saidaminov, S.I. Seok, M.D. McGehee, E.H. Sargent, H. Han, Challenges for commercializing perovskite solar cells, Science 361 (6408) (2018) eaat8235.

[26] J.-P. Correa-Baena, M. Saliba, T. Buonassisi, M. Grätzel, A. Abate, W. Tress, A. Hagfeldt, Promises and challenges of perovskite solar cells, Science 358 (6364) (2017) 739–744.

[27] M. Burresi, F. Pratesi, F. Riboli, D.S. Wiersma, Complex photonic structures for light harvesting, Adv. Opt. Mater. 3 (6) (2015) 722–743.

[28] H.V. Demir, S.V. Gaponenko, Applied Nanophotonics, Cambridge University Press, 2019.

[29] D.H. Kim, J.J. Kim, D.-J. Kong, G.J. Lee, Y.M. Song, Bio-inspired tunable optics and photonics: bridging the gap between nature and technology, Int. J. Optomech. 18 (1) (2024) 2334293.

[30] H. Zhou, J. Xu, X. Liu, H. Zhang, D. Wang, Z. Chen, D. Zhang, T. Fan, Bio-inspired photonic materials: Prototypes and structural effect designs for applications in solar energy manipulation, Adv. Funct. Mater. 28 (24) (2018) 1705309.

[31] S. Chakraborty, D. Bera, L. Roy, C.K. Ghosh, Biomimetic and bioinspired nanostructures: recent developments and applications, Bioinspir. Green Synth. Nanostruct.: Sustain. Approach (2023) 353–404.

[32] Y. Wang, P. Liu, F. Vogelbacher, M. Li, Bioinspired multiscale optical structures towards efficient light management in optoelectronic devices, Mater. Today Nano 19 (2022) 100225.

[33] R. Senthil, S. Yuvaraj, A comprehensive review on bioinspired solar photovoltaic cells, Int. J. Energy Res. 43 (3) (2019) 1068–1081.

[34] J. Yoon, Y. Hou, A.M. Knoepfel, D. Yang, T. Ye, L. Zheng, N. Yennawar, M. Sanghadasa, S. Priya, K. Wang, Bio-inspired strategies for next-generation perovskite solar mobile power sources, Chem. Soc. Rev. 50 (23) (2021) 12915–12984.

[35] V. Mascoli, A.F. Bhatti, L. Bersanini, H. van Amerongen, R. Croce, The antenna of far-red absorbing cyanobacteria increases both absorption and quantum efficiency of Photosystem II, Nature Commun. 13 (1) (2022) 3562.

[36] E.H. Harris, Chlamydomonas Sourcebook, vol. 2, Academic Press San Diego, 1989.

[37] F. Cariti, M. Chazaux, L. Lefebvre-Legendre, P. Longoni, B. Ghysels, X. Johnson, M. Goldschmidt-Clermont, Regulation of light harvesting in *Chlamydomonas reinhardtii* two protein phosphatases are involved in state transitions, Plant Physiol. 183 (4) (2020) 1749–1764.

[38] R.N. Burton-Smith, A. Watanabe, R. Tokutsu, C. Song, K. Murata, J. Minagawa, Structural determination of the large photosystem II–light-harvesting complex II supercomplex of *Chlamydomonas reinhardtii* using nonionic amphipol, J. Biol. Chem. 294 (41) (2019) 15003–15013.

[39] X. Su, J. Ma, X. Pan, X. Zhao, W. Chang, Z. Liu, X. Zhang, M. Li, Antenna arrangement and energy transfer pathways of a green algal photosystem-I–LHCI supercomplex, Nat. Plants 5 (3) (2019) 273–281.

[40] A.A. Tabrizi, A. Pahlavan, Efficiency improvement of a silicon-based thin-film solar cell using plasmonic silver nanoparticles and an antireflective layer, Opt. Commun. 454 (2020) 124437.

[41] F. Liu, Q. Zeng, J. Li, X. Hao, A. Ho-Baillie, J. Tang, M.A. Green, Emerging inorganic compound thin film photovoltaic materials: Progress, challenges and strategies, Mater. Today 41 (2020) 120–142.

[42] M. Beye, D. Diouf, B. Dieng, A.S. Maiga, Nanostructured silicon for antireflection and light trapping in crystalline silicon solar cells, in: Handbook of Nanomaterials for Manufacturing Applications, Elsevier, 2020, pp. 149–173.

[43] E.T. Efaz, M.M. Rhaman, S. Al Imam, K.L. Bashar, F. Kabir, M.E. Mourtaza, S.N. Sakib, F.A. Mozahid, A review of primary technologies of thin-film solar cells, Eng. Res. Express 3 (3) (2021) 032001.

[44] G.Y. Abdel-Latif, M.F.O. Hameed, M. Hussein, M.A. Razzak, S.S. Obayya, Electrical characteristics of funnel-shaped silicon nanowire solar cells, J. Photon. Energy 7 (4) (2017) 047501–047501.

[45] R. Pietruszka, B. Witkowski, E. Zielony, K. Gwozdz, E. Placzek-Popko, M. Godlewski, ZnO/Si heterojunction solar cell fabricated by atomic layer deposition and hydrothermal methods, Sol. Energy 155 (2017) 1282–1288.

[46] H. Sai, T. Matsui, K. Matsubara, Stabilized 14.0%-efficient triple-junction thin-film silicon solar cell, Appl. Phys. Lett. 109 (18) (2016).

[47] M. Green, E. Dunlop, J. Hohl-Ebinger, M. Yoshita, N. Kopidakis, X. Hao, Solar cell efficiency tables (version 57), Prog. Photovolt., Res. Appl. 29 (1) (2021) 3–15.

[48] M.A. Green, Polycrystalline silicon on glass for thin-film solar cells, Appl. Phys. A 96 (2009) 153–159.

[49] P. Sonntag, N. Preissler, M. Bokalič, M. Trahms, J. Haschke, R. Schlatmann, M. Topič, B. Rech, D. Amkreutz, Silicon solar cells on glass with power conversion efficiency above 13% at thickness below 15 micrometer, Sci. Rep. 7 (1) (2017) 873.

[50] S. Shestakov, E. Karbysheva, The origin and evolution of cyanobacteria, Biol. Bull. Rev. 7 (2017) 259–272.

[51] Z. Huang, L. Shen, W. Wang, Z. Mao, X. Yi, T. Kuang, J.-R. Shen, X. Zhang, G. Han, Structure of photosystem I-LHCI-LHCII from the green alga *Chlamydomonas reinhardtii* in state 2, Nature Commun. 12 (1) (2021) 1100.

[52] A.F. Oskooi, D. Roundy, M. Ibanescu, P. Bermel, J.D. Joannopoulos, S.G. Johnson, MEEP: A flexible free-software package for electromagnetic simulations by the FDTD method, Comput. Phys. Comm. 181 (3) (2010) 687–702.

[53] S. Baruah, J. Bora, S. Maity, Investigation and optimization of light trapping through hexagonal-shaped nanopillar (NP) array of indium gallium arsenide material based photodetector, Opt. Quantum Electron. 52 (8) (2020) 380.

[54] M. Nie, Y. Zhao, W. Nam, J. Song, W. Zhu, H.J. Lezec, A. Agrawal, W. Zhou, Broadband nanoscale surface-enhanced Raman spectroscopy by multiresonant nanolaminate plasmonic nanocavities on vertical nanopillars, Adv. Funct. Mater. 32 (32) (2022) 2202231.

[55] Z. Wang, R. Zhang, S. Wang, M. Lu, X. Chen, Y. Zheng, L. Chen, Z. Ye, C. Wang, K. Ho, Broadband optical absorption by tunable mie resonances in silicon nanocone arrays, Sci. Rep. 5 (1) (2015) 7810.

[56] S.L. Diedenhofen, O.T. Janssen, G. Grzela, E.P. Bakkers, J. Gòmez Rivas, Strong geometrical dependence of the absorption of light in arrays of semiconductor nanowires, ACS Nano 5 (3) (2011) 2316–2323.

[57] P. Spinelli, M. Verschuuren, A. Polman, Broadband omnidirectional antireflection coating based on subwavelength surface Mie resonators, Nat. Commun. 3 (1) (2012) 692.

[58] O.L. Muskens, J.G. Rivas, R.E. Algra, E.P. Bakkers, A. Lagendijk, Design of light scattering in nanowire materials for photovoltaic applications, Nano Lett. 8 (9) (2008) 2638–2642.

[59] American Society for Testing and Materials. Committee G03 on Weathering and Durability, Standard tables for reference solar spectral irradiances: direct normal and hemispherical on 37° tilted surface, ASTM international, 2003.

[60] E. Lohmüller, S. Werner, M.H. Norouzi, S. Gutscher, M. Demant, P. Saint-Cast, M. Linse, B. Bitnar, P. Palinginis, H. Neuhaus, et al., Low-ohmic contacting of laser-doped p-type silicon surfaces with pure Ag screen-printed and fired contacts, Phys. Status Solidi (A) 214 (12) (2017) 1700587.

[61] P. Vinod, Specific contact resistance and metallurgical process of the silver-based paste for making ohmic contact structure on the porous silicon/p-Si surface of the silicon solar cell, J. Mater. Sci., Mater. Electron. 21 (2010) 730–736.

[62] Lumerical Inc., FDTD: 3D electromagnetic simulator & CHARGE: 3D charge transport simulator, 2020, https://www.lumerical.com/.

[63] Lumerical Inc., Optoelectronic modeling, 2020, https://www.lumerical.com/learn/whitepapers/optoelectronic-modeling/.

[64] F. Sischka, GUMMEL-POONBIPOLARMODEL, Vol. 86, Agilent Technologies, Munich, 1990.

[65] D.A. Neamen, D. Biswas, Semiconductor Physics and Devices, McGraw-Hill Higher Education, New York, 2011.

[66] S.D. Nehate, A. Prakash, P.D. Mani, K.B. Sundaram, Work function extraction of indium tin oxide films from MOSFET devices, ECS J. Solid State Sci. Technol. 7 (3) (2018) P87.

[67] W. Fang, Z. Ni, P. Wang, C. Xiang, T. Sun, J. Zhang, R. Wang, J. Yang, Y. Yang, The ideal doping concentration of silicon wafer for single junction hybrid n-Si/PEDOT: PSS solar cells with 3.2% elevated PCE and V_{oc} of 620 mV, J. Mater. Sci., Mater. Electron. 31 (2020) 6398–6405.

[68] M. Savadogo, A. Ouedraogo, B. Soro, Z.D. Koudougou, M. Zoungrana, I. Zerbo, Analysis and comparison of doping level effects on a crystalline silicon PV cell under both moderate light concentration and normal illumination modes, Energy Power Eng. 14 (10) (2022) 523–540.

[69] W. Sugimura, T. Ono, S. Umeno, M. Hourai, K. Sueoka, Defect formation behaviors in heavily doped Czochralski silicon, ECS Trans. 2 (2) (2006) 95.

[70] C. Ballif, F.-J. Haug, M. Boccard, P.J. Verlinden, G. Hahn, Status and perspectives of crystalline silicon photovoltaics in research and industry, Nat. Rev. Mater. 7 (8) (2022) 597–616.

[71] M.-D. Ko, T. Rim, K. Kim, M. Meyyappan, C.-K. Baek, High efficiency silicon solar cell based on asymmetric nanowire, Sci. Rep. 5 (1) (2015) 11646.
[72] C. Zhang, L. Chen, Y. Zhu, Z. Guan, Fabrication of 20.19% efficient single-crystalline silicon solar cell with inverted pyramid microstructure, Nanoscale Res. Lett. 13 (2018) 1–8.
[73] J. Liu, X. Zhang, M. Ashmkhan, G. Dong, Y. Liao, B. Wang, T. Zhang, F. Yi, Fabrication and photovoltaic properties of silicon solar cells with different diameters and heights of nanopillars, Energy Technol. 1 (2–3) (2013) 139–143.
[74] H. Sai, K. Maejima, T. Matsui, T. Koida, M. Kondo, S. Nakao, Y. Takeuchi, H. Katayama, I. Yoshida, High-efficiency microcrystalline silicon solar cells on honeycomb textured substrates grown with high-rate VHF plasma-enhanced chemical vapor deposition, Japan. J. Appl. Phys. 54 (8S1) (2015) 08KB05.
[75] M.J. Keevers, T.L. Young, U. Schubert, M.A. Green, 10% Efficient CSG min-imodules, in: 22nd European Photovoltaic Solar Energy Conference, Vol. 3, (September) 2007, pp. 1783–1790.
[76] X. Liang, L. Shu, H. Lin, M. Fang, H. Zhang, G. Dong, S. Yip, F. Xiu, J.C. Ho, Inverted silicon nanopencil array solar cells with enhanced contact structures, Sci. Rep. 6 (1) (2016) 34139.